This is a peer-reviewed, author's accepted manuscript of the following conference paper: Duman, S., Boulougouris, E., Aung, M. Z., Xu, X., & Nazemian, A. (2023). *Numerical analysis of the impact of the bow thruster opening on a fast catamaran's resistance*. Paper presented at The 8th International Symposium on Ship Operations, Management and Economics, Athens, Greece. https://doi.org/10.5957/some-2023-034

# Numerical analysis of the impact of the bow thruster opening on a fast catamaran's resistance

**Suleyman Duman**[1], **Evangelos Boulougouris**[1,*], **Myo Zin Aung**[1], **Xue Xu**[1], **Amin Nazemian**[1]
1. Department of Naval Architecture, Ocean and Marine Engineering, University of Strathclyde, United Kingdom
*Corresponding Author: evangelos.boulougouris@strath.ac.uk

*Steering a ship in confined waters is particularly important for the efficient operation of high-speed ferries. Bow thruster is the obvious solution. It may have however an adverse effect on the resistance of the vessel. The interference between demihulls in the case of catamarans becomes an important and complex phenomenon as it affects many aspects of the hydrodynamic performance of the vessel. This study has focused on the analysis of the fluid flow around a fast catamaran with/without a bow thruster tunnel. A zero-carbon fast passenger ferry catamaran hull has been subjected to resistance simulations at two different speeds. Firstly, the catamaran hull without a bow opening has been simulated by commercial RANS solver software. After that, the simulations have been repeated for the catamaran hull with bow thruster opening. Finally, the bow opening has been filled with a gridded plane for garbage straining. The findings are very interesting for the fast catamaran ferry designers and operators. They are discussed for all three conditions in a comparative approach.*

KEY WORDS: Wave Interference; Catamaran; Bow Thruster; Bow Opening; CFD.

## NOMENCLATURE

| | |
|---|---|
| B, BM | Beam moulded (m) |
| BCs | Boundary conditions |
| BTT | Bow thruster tunnel |
| CF | Correction Factor |
| CF | Frictional resistance coefficient |
| CFD | Computational Fluid Dynamics |
| CP | Pressure coefficient |
| CR | Residual resistance coefficient |
| CT | Total resistance coefficient |
| DC372 | Delft Catamaran 372 |
| DoF | Degree-of-freedom |
| Fr, Fn | Froude Number |
| FS | Factors of Safety |
| g | Gravitational acceleration (m s-2) |
| GCI | Grid Convergence Index |
| H2020 | Horizon 2020 |
| ITTC | International Towing Tank Conference |
| KB | Vertical Centre of Buoyancy |
| L, LPP | Length between perpendiculars (m) |
| LC | Loading Condition |
| LCB | Longitudinal Centre of Buoyancy |
| LCB | Longitudinal Centre of Buoyancy |
| LWL | Length of waterline (m) |
| P | Pressure (N m-2) |
| Q | Pitch amplitude (deg) |
| R | Convergence condition |
| RANS | Reynolds-averaged Navier-Stokes |
| S | Wetted hull surface area (m2) |
| T | Draught at midship (m) |
| TrAM | Transport: Advanced and Modular |
| u, v, w | Fluid velocity components |
| VoF | Volume of Fluid |
| W/O-BTT | Without bow thruster tunnel |
| W-BTT | With bow thruster tunnel only |
| W-BTT+PL | With bow thruster tunnel and plate |
| W-PLATE | With bow thruster tunnel and plate |
| y+ | Dimensionless wall distance |
| Z | Heave amplitude (m) |
| ∇ | Displacement volume (m3) |
| α | Constant |
| ε | Relative error (%) |
| ζ | Wave height (m) |
| ρ | Density of water (kg m-3) |
| υ | Kinematic viscosity (N s m-2) |

## INTRODUCTION

Manoeuvrability in inland waters is a safety concern and can be overcome by applying relatively less complicated engineering solutions to marine vessels. Different types of propulsion systems have always been of interest to naval architects to improve the motion flexibility of floating bodies. A bow thruster is one of the most interesting control units with its obvious and superior features. Direct side forces can be generated by this unit which has a significant moment arm to the centre of gravity. As the design is naturally compromising course, the adverse effects of any positive achievements should be taken into account. The wave interference in the case of catamarans carries the problem to an interesting level. The asymmetric fluid flow in

the inner and outer regions of catamarans attracts scientific and industrial parties to investigate this phenomenon for both global characteristics, e.g., resistance, and motion; and local features, e.g., flow structure around a specific area on the hull surface.

The last two decades have brought a crucial and effective perspective, high-fidelity solution techniques, to the field of marine hydrodynamics. The CFD method has proved its validity, robustness, and powerful flexibility to analyse physical problems in virtual environments. Although the multihull vessel concept dates back many years ago, technical approaches to understanding the capabilities of such vessels were conducted starting late 20th century. As the concept is studied, bow thruster is emerged and begun to be investigated. The following studies can be given as examples to reflect the evolving steps: Symmetric catamarans were investigated regarding resistance performance by (Molland et al., 1994). Wave-making resistance and interference effects were analysed by (Insel and Doctors, 1995). An experimental study was conducted by (Van't Veer, 1998) to investigate the resistance and seakeeping characteristics of the Delft catamaran (DC372). Seakeeping performance of DC372 in rough seas was further studied by (Castiglione et al., 2011) with the help of URANS (unsteady Reynolds-averaged Navier-Stokes) equations solver. The studies on multihulls and bow thrusters have been further studied in the following studies: (Milanov et al., 2012) developed a manoeuvring model that is a function of advance speed and water depth for a water-jet-driven fast catamaran; (Duman and Bal, 2019) predicted the manoeuvring coefficients of a fast catamaran by conducting CFD simulations; (Yukun et al., 2020) presented a study on bow opening fairing and its effects on the hydrodynamic performance of a monohull by comparing single and multiple bow thruster design options; (Papanikolaou et al., 2020) presented a study focuses on the hydrodynamic hull form optimization of a zero emission, battery driven, fast catamaran vessel; (Boulougouris et al., 2021) presented the implementation of state-of-the-art "Industry 4.0" methods and tools to enable a fully electrical, fast zero-emission waterborne urban transport; (Shi et al., 2021) conducted an extensive study to predict the shallow water effects acting on a zero-carbon fast passenger catamaran; (Duman and Bal, 2022) applied the CFD method to DC372 to develop a non-linear manoeuvring mathematical model that can work at relatively high Froude numbers.

This study has been conducted as part of an ongoing Horizon 2020 (H2020) project TrAM: Transport, Advanced and Modular (TrAM, 2022), in order to investigate the effects of the bow thruster tunnel on the hydrodynamic performance of the Stavanger Demonstrator of TrAM at a moderate and high speed. The Stavanger Demonstrator has been subjected to 2-DoF (degree-of-freedom) CFD (computation fluid dynamics) simulations for the following design options: without a bow thruster tunnel (WO-BTT), with a bow thruster tunnel fully open (W-BTT or WO-PLATE), and finally, bow thruster with a plate of four small circular holes (W-BTT+PL or W-PLATE). The computational results have been discussed through numerical and visual examinations. Significant findings have been reported and detailed visual media have been presented to provide comparison data for future studies.

# MATHEMATICAL MODELS

## Geometric Properties of The Catamaran Hull

The catamaran hull form is designed for carrying passengers with fully electric power as part of an ongoing EU-funded project TrAM (TrAM, 2022). The first demonstrator of the TrAM project, Stavanger Demonstrator, was launched and named MS Medstraum in Stavanger, Norway, to provide zero-emission transportation with a maximum of 27 kn recorded speed. The Stavanger Demonstrator is a special design for being the world's first 100% battery-driven fast passenger ferry.

The catamaran hull form consists of two symmetrical slender demihulls, an axe-shaped bow, and a transom stern (Fig. 1). To reduce the number of interactions, the un-appended Stavanger Demonstrator is used in this study to focus on the hull-BTT interactions.

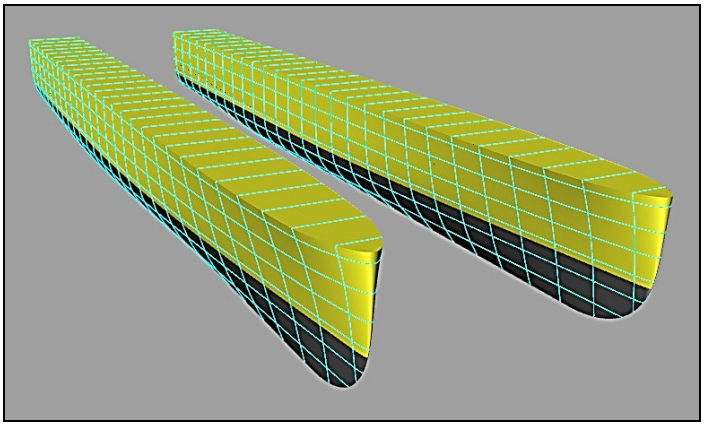

Fig. 1: Catamaran hull 3-D surface from the perspective view.

The main dimensions of the Stavanger Demonstrator are given in Table 2.1 in nondimensional form. The separation (s) refers to the distance between the centrelines of demihulls. The loading condition (LC) is specified by the nondimensional draught.

Table 1: Principal dimensions of the Stavanger Demonstrator.

| Dimension | Nondim. | Nondim. Value |
|---|---|---|
| Separation (s) | s/Lpp | 0.227 |
| Draught (T) | T/Lpp | 0.046 |
| KB | KB/Lpp | 0.026 |
| LCB | LCB/Lpp | 0.460 |

## Computational Method

All the CFD simulations of the Stavanger Demonstrator reported here have been performed at model scale by using the commercial RANS solver software Star-CCM+ (Simcenter Star-CCM+, 2022). This chapter presents the governing equations, boundary conditions, discretization of the computational

domain, and the nondimensionalisation procedure followed in this study.

***Governing equations*** In CFD simulations, the catamaran hull is allowed to move freely on a vertical plane passing by the longitudinal symmetry centre. The multiphase flow field has been modelled by implementing the VoF (volume of fluid) method (Hirt and Nichols, 1981). The initial state of the free water surface is assumed undisturbed where the ship floats at the specified LC.

The fluid flow inside the computational domain is assumed to be Newtonian, incompressible and turbulent. The following equations are solved to achieve the multi-phase flow simulations: the continuity equation (Equation 1) and the Reynolds-averaged Navier-Stokes (RANS) equations (Equation2) in an unsteady way. As a result of averaging operation to the original Navier-Stokes (momentum) equations, Reynolds stresses (Equation 3) appears that are modelled by the turbulence model. The near-wall treatment is activated within the turbulence model, Realizable k-epsilon, by setting the dimensionless wall distance (y+) to be between 30-300 which enables the wall function near the no-slip walls. Timestep, one of the key parameters for well-posed unsteady solutions, is determined according to the ITTC recommendations following the Equation 4 and is kept constant as all the computations are based on the implicit solution algorithm (ITTC, 2011).

$$\frac{\partial(\bar{u}_i)}{\partial x_i} = 0 \tag{1}$$

$$\frac{\partial(\bar{u}_i)}{\partial t} + \bar{u}_j \frac{\partial(\bar{u}_i)}{\partial x_j} + \frac{\partial(\overline{u'_i u'_j})}{\partial x_j} = -\frac{1}{\rho}\frac{\partial \bar{p}}{\partial x_j} + \frac{\partial \bar{\tau}_{ij}}{\partial x_j} \tag{2}$$

$$\bar{\tau}_{ij} = \nu\left(\frac{\partial \bar{u}_i}{\partial x_j} + \frac{\partial \bar{u}_j}{\partial x_i}\right) \tag{3}$$

$$\Delta t = 0.005 \div 0.01\frac{L}{V} \tag{4}$$

***Computational domain boundaries and grid resolution*** The sizes of the computational domain mainly depend on the type of the physical problem. Dimensions should provide adequate clearance for the initialization of the solution and for the developing flow without having an undesired numerical error. When previous CFD studies are searched, it is seen that at least 1.5L upstream, 3L downstream and 2L clearance are very common and give sufficient enough space to allow free surface waves to be developed for conventional resistance simulations (Castiglione et al., 2011; Duman and Bal, 2022; He et al., 2011; Shi et al., 2021). Bottom and top boundaries are generally assigned 1L to 1.5L far from the floating body. By considering previous experiences and recommendations and customise them to Stavanger Demonstrator, 2.37L and 3.75L distances are set for the CFD simulations in the upstream and downstream directions, respectively. Since there is no superstructure in the model geometry the top boundary is located 1.68L far in height from the origin of the coordinate system which is assigned at the intersection point of the aft perpendicular and the keel of the vessel. The side boundaries are located about 2.25L away from the centreline (Table 2). To avoid the bank effects in deep water simulations, an artificial infinite boundary effect is achieved by setting top and bottom faces as inlets where the fluid flows in the longitudinal direction, and yet no flux enters the domain from these faces.

Table 2: Computational domain dimensions in CFD simulations.

| Boundaries | Background (*L) |
|---|---|
| Upstream | 2.370 |
| Downstream | 3.745 |
| Top | 1.685 |
| Bottom | 1.685 |
| Side | 2.247 |

The boundary conditions that are used in CFD simulations are shown in Fig. 2. The computational domain is divided into two main regions: Background and overset. In the background domain: Front, top, bottom and side faces are assigned as velocity inlets; back face is set to outlet; boundary face on the centreline of the catamaran is set to symmetry conditions. In the overset domain: All faces except the boundary face on the centreline, which is set to symmetry, are assigned as overset boundaries. The Stavanger Demonstrator hull is assigned as no-slip wall where the tangential and normal velocities are zero on the hull surface. The Chimera or overset facilitates large amplitude motions without any deformation on the grid cells around the moving body. The flow features such as velocity and pressure, are transferred between the overset boundaries and the background overlapping cells through the intersecting points.

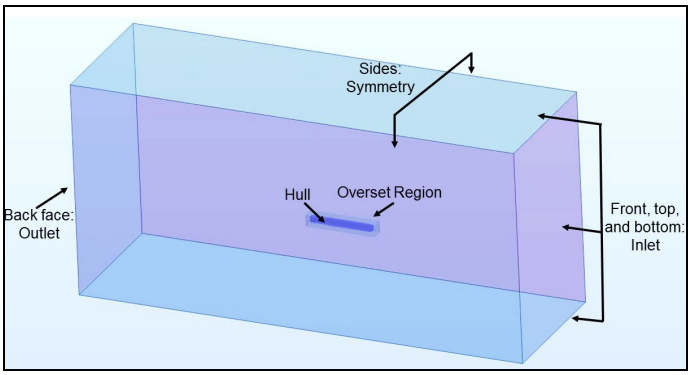


Fig. 2: Boundary conditions in CFD simulations of the catamaran.

The Chimera or overset grid technique can provide high accurate dynamic solutions without any deformation on the grid cells around the moving body on that matter. The flow field is divided into two main regions; background and overset, and the flow information is transferred between the boundaries of the overset region and the background region overlapping cells through the intersecting points (Benek et al., 1986). Coloured

representations of the grid cells and information about the data transfer between those cells for catamarans in CFD simulations can be found in the literature.

In multiphase marine hydrodynamic problems, the interaction field should be handled in the first place rather than the far field. The mesh structure in this study is designed to start finer near the no-ship surfaces and to continue with a rate of change to get coarser in the relatively far points. The inner field between the demihulls and the overset boundary sites are discretized with smaller cells to capture the wave interference well and to provide a smooth transfer of the flow data between background and overset regions (Fig. 3). The ideal way of discretizing the free water surface is to use very small and equally-sized cells on that horizontal plane. However, this approach will generate a very dense mesh and will be far more than practical and cost-effective due to the need for high computational power. Instead, a Kelvin-wave adopted grid has been applied in this study to capture the free surface deformations. The density of the grid resolution on the aft part and bow thruster tunnel of the Stavanger Demonstrator have been increased (Fig. 4).

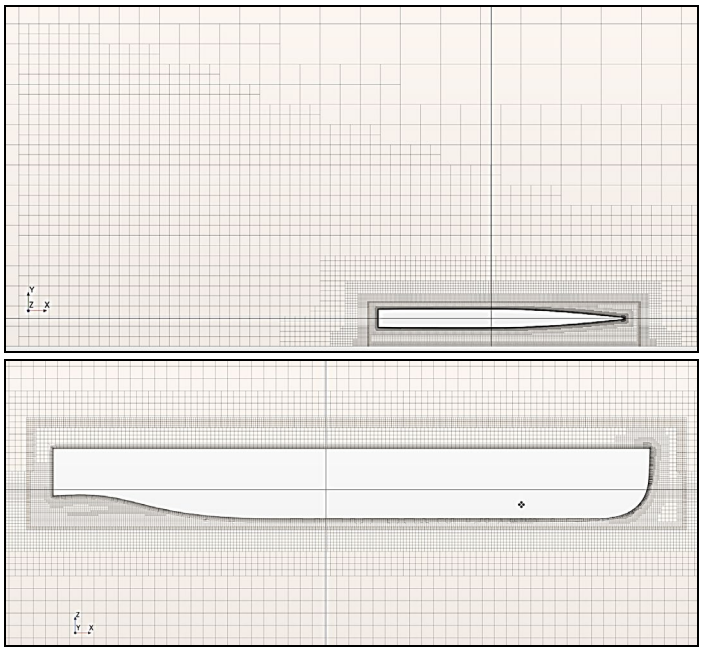

Fig. 3: Grid structure on the free water surface (upper) and the symmetry plane of a demi-hull (lower) in CFD simulations of the catamaran.

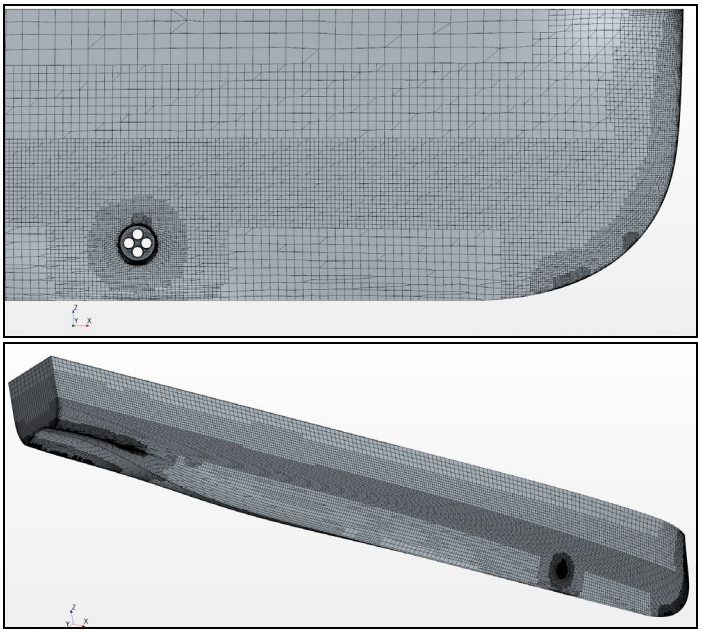

Fig. 4: Grid structure on the fully-appended Stavanger Demonstrator.

## Presentation of Data

The force units are nondimensionalised by following Equation 5 where it is necessary. X and Y represent and scalar force units, ρ is the fluid density, U is the ship advance speed and the S stands for the dynamic wetted surface area. The length units are nondimensionalized by the ship length. The experimental resistance results have been decomposed by subtracting the $C_F$ from the $C_T$ values that are calculated in CFD simulations (Equation 6). The corresponding Froude numbers are calculated using Equation 7 and provided in the tabulated results. The wave elevations on the hull surfaces are nondimensionalized by using Equation 9.

$$X',\ Y' = \frac{X,\ Y}{0.5\rho U^2 S} \tag{5}$$

$$C_T = C_F + C_R \tag{6}$$

$$Fr = \frac{U}{\sqrt{gL_{WL}}} \tag{7}$$

$$C_P = \frac{P}{0.5\rho U^2} \tag{8}$$

$$\zeta = \frac{U}{g^2} \tag{9}$$

# RESULTS AND DISCUSSION

### Uncertainty Assessment

The uncertainty analysis has been carried out by using the latest solution verification techniques based on Richardson extrapolation: Grid Convergence Index (GCI), Correction Factor (CF) and Factors of Safety (FS) (Roache, 1994; Stern et al., 2001; Xing and Stern, 2010). The total grid cell numbers are increased by changing the dimensions of the reference cell by

√2 as recommended by ITTC (ITTC, 2011). Since the verification procedure is applied to a 3-dimensional problem, the ratio between the total grid cell numbers of different qualities is defined as follows (Equation 10):

$$r_{21} = \left(\frac{N_1}{N_2}\right)^{1/3} \qquad r_{32} = \left(\frac{N_2}{N_3}\right)^{1/3} \tag{10}$$

where N1, N2 and N3 are the total cell numbers and N3 < N2 < N1. The difference between any numerical scalar result, which is total resistance in this case, between two different grid cells can be calculated as follows (Equation 11):

$$E_{21} = X_2 - X_1 \qquad E_{32} = X_3 - X_2 \tag{11}$$

The convergence condition of the numerical solution then can be observed by dividing the constants calculated in Equation 13: $R = E_{21}/E_{32}$. The mathematical meaning of the ratio R is described in Equation 12 and details can be found in the related reference (Phillips and Roy, 2014).

$$\begin{aligned} -1 < R < 0 &\quad \text{Oscillatory convergence} \\ 0 < R < 1 &\quad \text{Monotonic convergence} \\ R < -1 &\quad \text{Oscillatory divergence} \\ 1 < R &\quad \text{Monotonic divergence} \end{aligned} \tag{12}$$

Three different grid qualities have been tested at 0.30 Froude number to calculate the total resistance of the Stavanger Demonstrator at the specified LC (Table 3). For verification analysis, the W/O-BTT option has been chosen. The relative percentage between the fine and medium mesh has been calculated as 2.63%. Considering the computational cost, the medium mesh quality has been adopted for the rest of the simulations. Note that this relative difference should be taken into account together with the uncertainty amount in the computations to draw the limits of the outputs (Table 4).

Table 3: Resistance values at Fr=0.30 by different grid qualities.

| Grid quality | Total cell numbers | $C_T$ (*$10^3$) |
|---|---|---|
| Fine | 6.80E+06 | 4.5765 |
| Medium | 3.92E+06 | 4.6969 |
| Coarse | 2.37E+06 | 4.7950 |

The total resistance values are decreasing gradually as the grid resolution becomes dense. The convergence condition R which is the ultimate indication of the convergence type for Richardson-based verification methods, shows that the numerical solution reaches to a certain value monotonically. The highest uncertainty is calculated as 10% by the FS method.

Table 4: Uncertainty assessment results.

| | GCI | CF | FS |
|---|---|---|---|
| $r_{21}$ | 1.20 | 1.20 | 1.20 |
| $r_{32}$ | 1.18 | 1.18 | 1.18 |
| R | 0.73 | 0.73 | 0.73 |
| $P_{th}$ | 2.00 | 2.00 | 2.00 |
| $P_{RE}$ | 2.19 | 2.19 | 2.19 |
| $C_{T\text{-}Ext}$ (*$10^3$) | 6.213 | 6.213 | 6.213 |
| SF | 1.25 | 1.12 | 1.10 |
| Δ (%) | 3.90 | 3.86 | 10.01 |

The safety factors in uncertainty assessment are calculated as in Equation 13. Here, the theoretical order of accuracy Pth is taken as 2 for spatial uncertainty and the observed order of accuracy P is calculated according by using Equation 14

$$SF_{GCI} = 1.25,\ SF_{CF} = \frac{{r_{21}}^{P}-1}{{r_{21}}^{Pth}-1},\ SF_{FS} = \frac{P}{Pth} \tag{13}$$

$$P = \frac{ln(1/R)}{ln(r_{21})} \tag{14}$$

**Computational Analysis Results**

The Stavanger Demonstrator has been analysed for three different design options: (1) without a bow thruster tunnel (W/O-BTT), (2) with bow thruster opening only (denoted with W-BTT or W/O-PLATE), and (3) with bow thruster opening filled with a thin plate (W-BTT+PL or W-PLATE). The thin plate is formed by cutting four exact circular holes which have normal in lateral direction. The practical application of this thin plate can be seen in such vessel for garbage retaining. The CFD simulations have been performed at a moderate (Fn=0.30) and high speed (Fn=0.69). The resistance coefficients and motion amplitudes are tabulated in nondimensional form in Table 5 and Table 6, respectively. In all cases, the option 2, W-BTT, has the highest total resistance compared to other options. Since there is frictional resistance values are similar to each other, it can be deduced that the pressure-based resistance component is highly sensitive to a fully open bow thruster tunnel. The option 3, W-PLATE, has the lowest frictional values for all cases. The total resistance values for this design option are also very close to those obtained for the W/O-BTT option (Table 5). The options 2 and 3 force the catamaran hull downwards and increase the heave motion amplitude at both 0.30 and 0.69 Froude numbers. However, they suppress the trim values even though the absolute values are quite small (Table 6).

Table 5: Total resistance coefficients for different design options.

Table 6: Sinkage and trim values for different design options.

| Fn \ $C_T$* $10^3$ | $C_{T(W/O-BTT)}$ | $C_{T(W-BTT)}$ | $C_{T(W-BTT+PL)}$ | $C_{F(W/O-BTT)}$ | $C_{F(W-BTT)}$ | $C_{F(W-BTT+PL)}$ |
|---|---|---|---|---|---|---|
| 0.30 | 4.6969 | 5.4309 | 4.6817 | 2.9323 | 2.9286 | 2.8885 |
| 0.69 | 4.0334 | 4.6859 | 4.0427 | 2.4879 | 2.5076 | 2.4496 |

The pressure distributions are presented in Fig. 5 and 6 for 0.30 and 0.69 Froude numbers, respectively. In both Figures, captions are set to the same aspect ratio to present the same surface area for a better comparison, i.e., top-left captions show the same surface area with the other captions in those figures. It is seen that the W-BTT where there is no plate has higher pressure pick and drop on the top-edge of bow thruster opening (top-right captions in Fig. 5 and 6). These differences become even higher at 0.69 Froude number. The pressure field is highly disturbed when there is no plate in the bow opening. However, a plate of four circular holes (W-BTT+PL) has less adverse effects on the pressure distribution as the gradually decreasing pressure changes in the vertical direction are kept well compared to W/O-BTT.

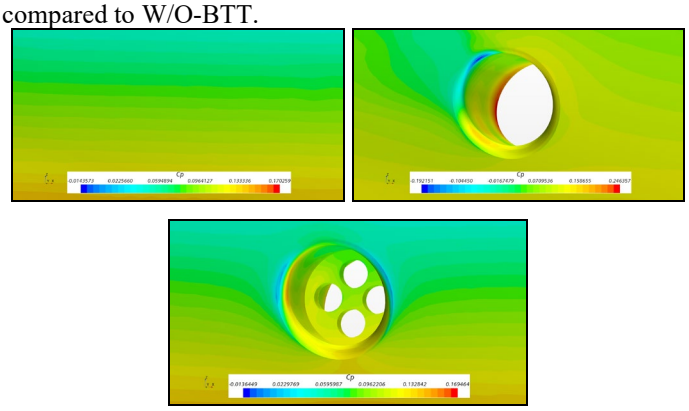

Fig. 5: Pressure distributions around the bow thruster opening at Fr=0.30: W/O-BTT (top-left), W-BTT (top-right) and W-BTT+PL (bottom).

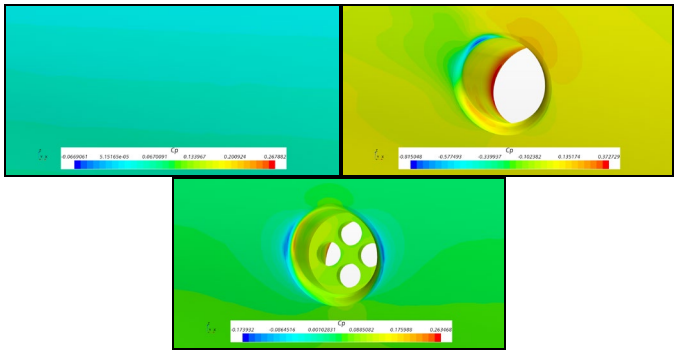

Fig. 6: Pressure distributions around the bow thruster opening at Fr=0.69: W/O-BTT (top-left), W-BTT (top-right) and W-BTT+PL (bottom).

The streamlines passing by the BTT area are presented in Figs. 7-12. In each figure, four captions are provided to help readers to understand the behaviour of the fluid flow in the outer region and inner region (interference field) of the catamaran hull. Closer-look captions are also presented on the right-hand side of each figures. Fig. 7 and Fig. 10 give the idea of how undisturbed streamlines are expected to be formed at 0.30 and 0.69 Froude numbers, respectively. Fig. 8 and Fig. 11 show the extreme behaviour of the streamlines entering the BTT on the outer surface and exit from the inner surface. Strong swirls have been reported when the tunnel is fully open. Fig. 9 and Fig. 12 have the streamlines captured for the W-BTT+PL design option where the streamlines are still disturbed, however, the general characteristics and order of the streamlines are mostly well-kept. Even though the W-BTT+PL option has still four circular holes, blocking the BTT to a certain extend has significantly less adverse effects than the fully open version.

At both advance speeds, 0.30 and 0.69 Froude numbers, the streamlines move from the outer field to the inference region between demihulls. The interactions in this field result in channel effects which accelerate the flow and create a suction side that leads to swirls (Fig. 8 and Fig. 11). A partly filled bow thruster tunnel blocks these swirls effectively and holds fluid flow inside the tunnel and behaves as a solid boundary which leads to more structured flow characteristics with less disturbance (Fig. 9 and Fig. 12).

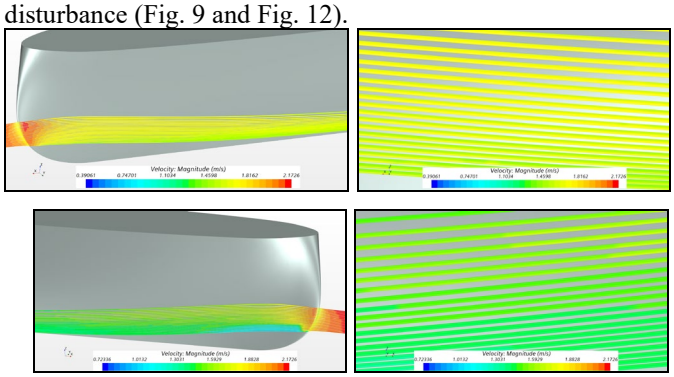

Fig. 7: Streamlines passing BTT area at Fr=0.30 w/o the opening: outer surface (top-left), outer surface closer look (top-right); inner surface (bottom-left), inner surface closer look (bottom-right).

| Fn \ Z'*$10^3$, Q | Z'$_{(W/O-BTT)}$ | Z'$_{(W-BTT)}$ | Z'$_{(W-BTT+PL)}$ | Q$_{(W/O-BTT)}$ | Q$_{(W-BTT)}$ | Q$_{(W-BTT+PL)}$ |
|---|---|---|---|---|---|---|
| 0.30 | -1.2487 | -1.4049 | -1.3314 | -0.0365 | -0.0093 | -0.0144 |
| 0.69 | 0.0340 | -0.1191 | -0.0118 | -1.0588 | -1.0027 | -1.0440 |

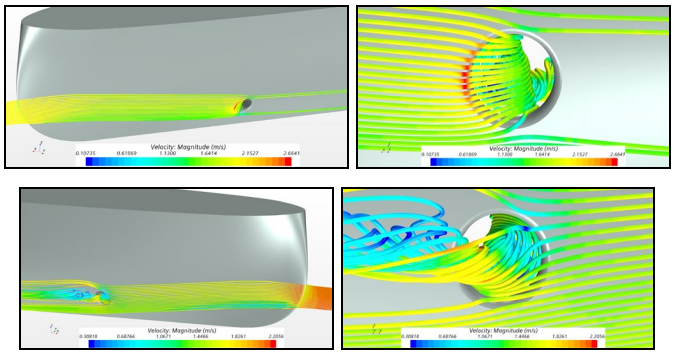

Fig. 8: Streamlines passing BTT area at Fr=0.30 with the opening: outer surface (top-left), outer surface closer look (top-right); inner surface (bottom-left), inner surface closer look (bottom-right).

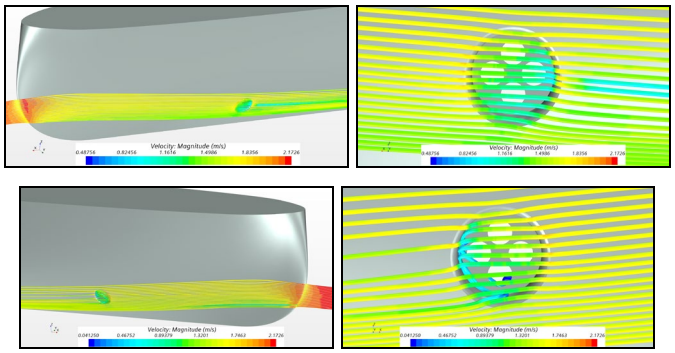

Fig. 9: Streamlines passing BTT area at Fr=0.30 with the opening and plate: outer surface (top-left), outer surface closer look (top-right); inner surface (bottom-left), inner surface closer look (bottom-right).

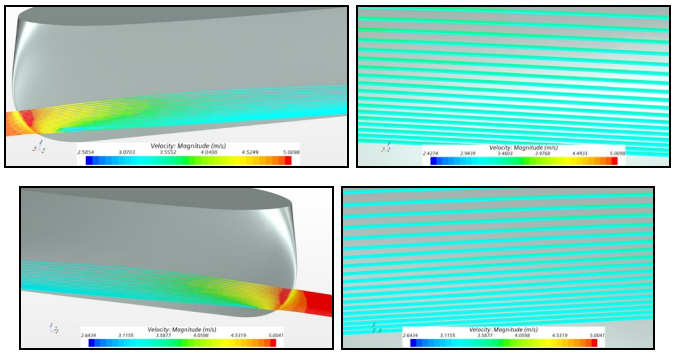

Fig. 10: Streamlines passing BTT area at Fr=0.69 w/o the opening: outer surface (top-left), outer surface closer look (top-right); inner surface (bottom-left), inner surface closer look (bottom-right).

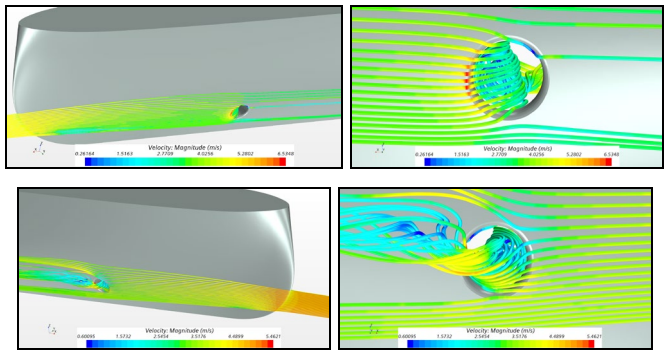

Fig. 11: Streamlines passing BTT area at Fr=0.69 with the opening: outer surface (top-left), outer surface closer look (top-right); inner surface (bottom-left), inner surface closer look (bottom-right).

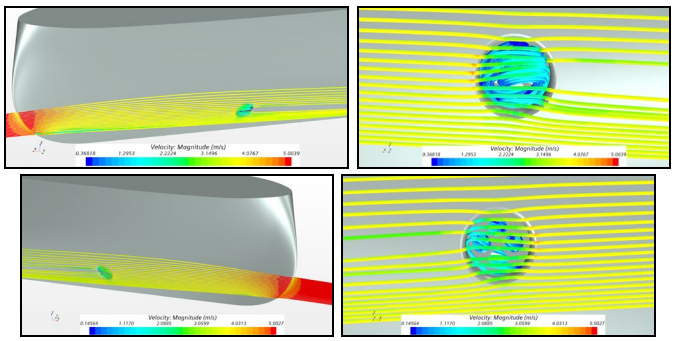

Fig. 12: Streamlines passing BTT area at Fr=0.69 with the opening and plate: outer surface (top-left), outer surface closer look (top-right); inner surface (bottom-left), inner surface closer look (bottom-right).

Wavecuts on both sides of a demihull have been plotted compared to each other. Top captions in Fig. 13 show the wavecuts captured at 0.30 Froude number. The outer surface stands for the hull surface in the outside region while inner surface refers to the hull surface that faces the fluid flow in the interference region (field between demihulls). The horizontal axis is the normalized longitudinal axis (x'=1 is the bow and x'=0 is the stern of the catamaran hull) and the vertical axis is the nondimensional wave elevation. The steady-state wave profiles on the outer and inner regions are in line with the streamline characteristics. It is clear that the W/O-BTT and W-BTT+PL results have excellent match while W/O-PLATE disturbs the free surface above of BTT.

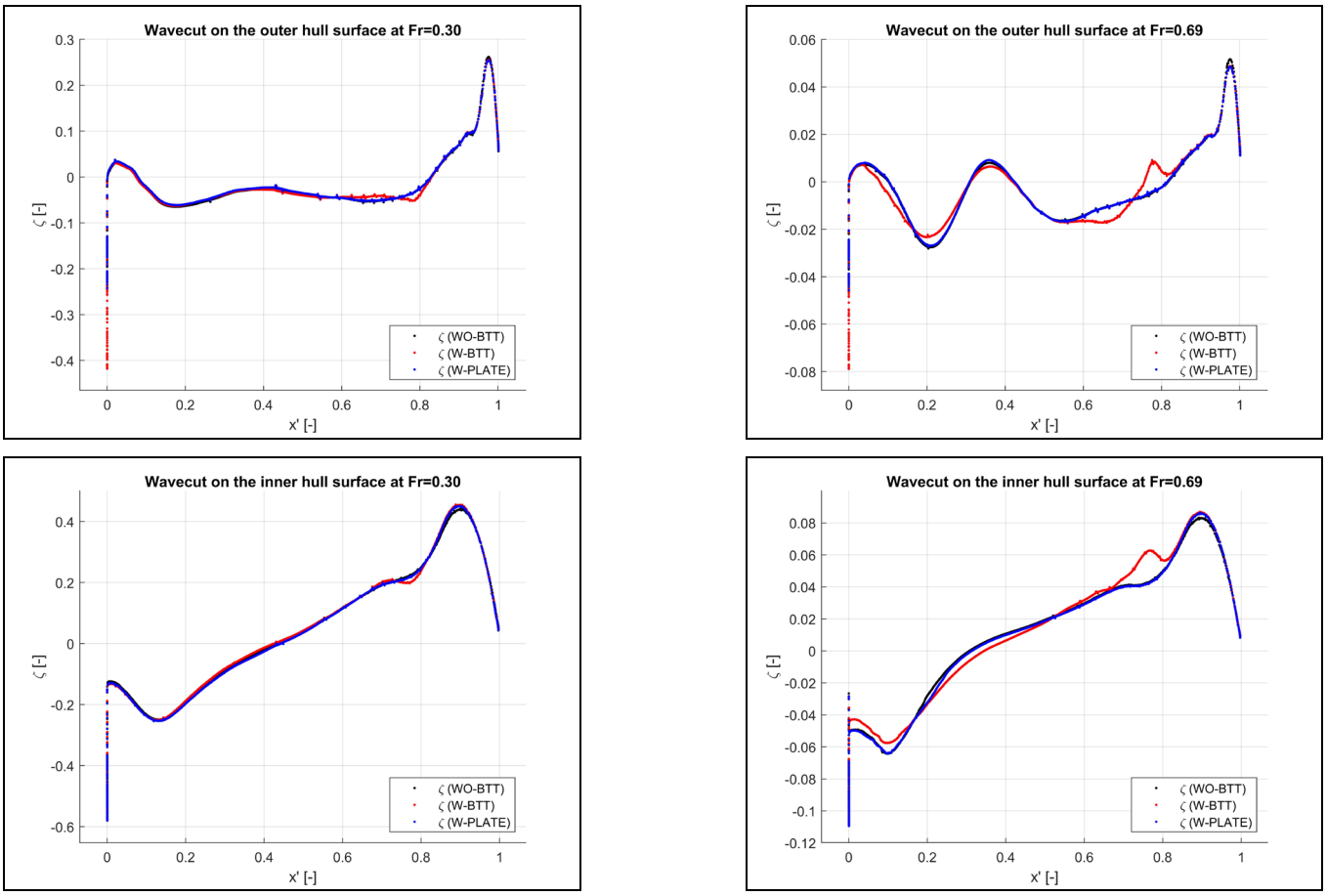


Fig. 13: Wavecuts on the inner and outer hull surfaces at Fr=0.30 (top-left&right) and Fr=0.69 (bottom-left&right).

## CONCLUSIONS

This study has been conducted to look for insight into the bow thruster tunnel effects on the hydrodynamic performance of a zero-emission fast catamaran ferry. The subject vessel, the Stavanger Demonstrator catamaran hull, was built and named MS Medstraum in Norway as a demonstrator of an ongoing H2020 project TrAM.

The catamaran has been analysed under free surface effects in deep water at two different operation speeds. For each speed, three configurations have been investigated: W/O-BTT, W-BTT and W-BTT+PL. Detailed visual examination of the problem has been presented. The CFD results show that a completely open bow thruster tunnel has extreme adverse effects on the streamlines passing by the BTT area. The swirls that pass the BTT elevate the free surface in the inner region which should be taken into consideration when freeboard height is a design parameter. However, a plate can increase the performance significantly. No matter which shape is used, a BTT forces the vessel to sink and to trim to bow. The main reason for higher total resistance values in W-BTT is the increase in pressure-based resistance component. Based on the results obtained for the presented design options, it is recommended that designers

should adopt partly or fully closed bow thruster tunnels to reduce the swirl effects and to have less disturbed streamlines.
The hydrodynamic performance of the Stavanger Demonstrator will be further investigated for different BTT shapes, shallow water and bow thruster interaction, and different loading conditions. The propeller effects will be taken into consideration in future studies.

## ACKNOWLEDGEMENTS

This work was funded by the H2020 European Union project "TrAM – Transport: Advanced and Modular" under the contract number 769303. The authors affiliated with MSRC greatly acknowledge the funding from DNV and Royal Caribbean Group for the MSRC's establishment and operation. The opinions expressed herein are those of the authors and do not reflect the views of DNV and Royal Caribbean Group. CFD simulations run by the University of Strathclyde were performed on ARCHIE-WeSt High Performance Computer (www.archie-west.ac.uk (accessed on 25 November 2022)).

## REFERENCES

Benek, J.A., Steger, J.L., Dougherty, F.C., Buning, P.G., 1986. Chimera: A Grid-Embedding Technique (No. AEDC-TR-85-64). Arnold Engineering Development Center, Arnold Air Force Station, Tennessee.

Boulougouris, E., Papanikolaou, A., Dahle, M., Tolo, E., Xing-Kaeding, Y., Jürgenhake, C., Seidenberg, T., Sachs, C., Brown, C., Jenset, F., 2021. Implementation of Zero Emission Fast Shortsea Shipping, in: SNAME Maritime Convention. OnePetro.

Castiglione, T., Stern, F., Bova, S., Kandasamy, M., 2011. Numerical investigation of the seakeeping behavior of a catamaran advancing in regular head waves. Ocean Eng. 38, 1806–1822. https://doi.org/10.1016/j.oceaneng.2011.09.003

Duman, S., Bal, S., 2022. Turn and zigzag manoeuvres of Delft catamaran 372 using CFD-based system simulation method. Ocean Eng. 264, 112265.

Duman, S., Bal, S., 2019. Prediction of maneuvering coefficients of Delft catamaran 372 hull form, in: Georgiev, P., Soares, C.G. (Eds.), Sustainable Development and Innovations in Marine Technologies. CRC Press, pp. 167–174. https://doi.org/10.1201/9780367810085-21

He, W., Castiglione, T., Kandasamy, M., Stern, F., 2011. URANS Simulation of Catamaran Interference. Presented at the 11th International Conference on Fast Sea Transportation FAST 2011, Honolulu, Hawaii, USA.

Hirt, C.W., Nichols, B.D., 1981. Volume of fluid (VOF) method for the dynamics of free boundaries. J. Comput. Phys. 39, 201–225. https://doi.org/10.1016/0021-9991(81)90145-5

Insel, M., Doctors, L.J., 1995. Wave pattern prediction of monohulls and catamarans in a shallow-water canal by linearised theory, in: Proceeding of 12 Th Australian Fluid Mechanics Conference. pp. 259–262.

ITTC, 2011. Practical Guidelines for Ship CFD Applications. Presented at the Proceedings of 26th ITTC, Rio de Janerio, Brazil.

Milanov, E., Chotukova, V., Stern, F., 2012. System Based Simulation of Delft372 Catamaran Maneuvering Characteristics as Function of Water Depth and Approach Speed. Presented at the 29th Symposium on Naval Hydrodynamics, Gothenburg, Sweden.

Molland, A., Wellicome, J., Couser, P., 1994. Resistance experiments on a systematic series of high speed displacement catamaran forms: variation of length-displacement ratio and breadth-draught ratio.

Papanikolaou, A., Xing-Kaeding, Y., Strobel, J., Kanellopoulou, A., Zaraphonitis, G., Tolo, E., 2020. Numerical and Experimental Optimization Study on a Fast, Zero Emission Catamaran. J. Mar. Sci. Eng. 8, 657. https://doi.org/10.3390/jmse8090657

Phillips, T.S., Roy, C.J., 2014. Richardson Extrapolation-Based Discretization Uncertainty Estimation for Computational Fluid Dynamics. J. Fluids Eng. 136, 121401. https://doi.org/10.1115/1.4027353

Roache, P.J., 1994. Perspective: A Method for Uniform Reporting of Grid Refinement Studies. J. Fluids Eng. 116, 405. https://doi.org/10.1115/1.2910291

Shi, G., Priftis, A., Xing-Kaeding, Y., Boulougouris, E., Papanikolaou, A.D., Wang, H., Symonds, G., 2021. Numerical Investigation of the Resistance of a Zero-Emission Full-Scale Fast Catamaran in Shallow Water. J. Mar. Sci. Eng. 9, 563. https://doi.org/10.3390/jmse9060563

Simcenter Star-CCM+, 2022. Simcenter Star-CCM+.

Stern, F., Wilson, R.V., Coleman, H.W., Paterson, E.G., 2001. Comprehensive Approach to Verification and Validation of CFD Simulations—Part 1: Methodology and Procedures. J. Fluids Eng. 123, 793. https://doi.org/10.1115/1.1412235

TrAM, 2022. Transport: Advanced and Modular (TrAM) Horizon2020 Project. [WWW Document]. URL https://tramproject.eu/ (accessed 11.28.22).

Van't Veer, R., 1998. Experimental results of motions, hydrodynamic coefficients and wave loads on the 372 catamaran model (Technical Report No. 1129). Delft University of Technology, Delft, The Netherlands.

Xing, T., Stern, F., 2010. Factors of Safety for Richardson Extrapolation. J. Fluids Eng. 132, 061403. https://doi.org/10.1115/1.4001771

Yukun, F., Zuogang, C., Yi, D., Zheng, Z., Ping, W., 2020. An experimental and numerical investigation on hydrodynamic characteristics of the bow thruster. Ocean Eng. 209, 107348. https://doi.org/10.1016/j.oceaneng.2020.107348